



**Duke University**  
**Environmental Physics Laboratory**  
**Civil and Environmental Engineering**  
**Pratt School of Engineering**

## **Report EPL-2019-IPHEX-H4SE-4**

### **IPHEX Series**

The Integrated Precipitation and Hydrology Experiment – Hydrologic Applications for the Southeast US (IPHEX-H4SE)

Part IV: High-Resolution Enhanced StageIV-Raingauge Combined Precipitation Product

**Merging Raingauge and Radar Measurements using Fractal Downscaling and Kriging**  
**The IPHEX QPE+ Rainfall Product**



<http://iphex.pratt.duke.edu>

Mochi Liao and Ana P. Barros  
EPL-2019-IPHEX-H4SE-4

June 18, 2019 – V1.0

## Abstract

This report is companion to Version 1 (V1) of the IPHEX (Integrated Precipitation and Hydrology Experiment) reference quantitative precipitation estimation (RQPE) product. The *IPHEX-QPE-1.1 V1* consists of 10 years (2008-2017) hourly rainfall intensity at  $1 \text{ km}^2$  resolution over the core region of the IPHEX domain, centered in the Pigeon River basin in The Southern Appalachian Mountains in North Carolina. Two data sets are the basis of the IPHEX RQPE: 1) the national combined radar-raingauge StageIV product (hourly,  $16\text{km}^2$  spatial resolution); and 2) independent raingauge measurements from a network of high elevation raingauges in the region installed in support of NASA TRMM and GPM ground validation (GV) activities. First, fractal downscaling is applied to the Stage IV product to bring it to the  $1 \text{ km}^2$  resolution ( $\text{STIV}_D$ ). Regional event bias correction is then applied to the hourly downscaled StageIV product ( $\text{STIV}_{DB}$ ), followed by ordinary kriging (OK) to distribute errors among  $\text{STIV}_{DB}$  and co-located raingauge observations to generate the final product  $\text{STIV}_{DBK}$ . Evaluation of  $\text{STIV}_{DBK}$  indicates that cumulative rainfall errors are as small as 1-3% while  $\text{STIV}_D$  data have errors about 10-15%. However, assessment against the 10-year raingauge climatology revealed that significant biases at specific times-of-the day remain in  $\text{STIV}_{DBK}$ , which also exhibit seasonality. These biases reflect radar operations and viewing geometry that have preferential impact for shallow precipitation systems and isolated intense convection. Consequently, light and convective rainfall corrections were applied to derive the final product ( $\text{STIV}_{DBKC}$ ) that is *IPHEX-QPE-1.1 V*. Performance metrics such as Threat Score (TS) and Heidke Skill Scores (HSS) are on average  $> 0.8$  and close to 1 respectively for various rainfall thresholds over the 10-year period, and  $> 0.5$  at the event time-scale(hourly). The root mean square error (RMSE) at the gauges is below 0.1 mm/hr and 0.5% for seasonal-scale accumulations. Evaluation against an independent disdrometer data set consisting of disdrometers at various locations indicates large overestimation errors ( $\sim 30\%$ ) in the inner mountain region and at low elevations during the IPHEX IOP. This is in part attributed to the lack of low elevation raingauges and the overshooting of both NEXRAD radars that contribute to the Stage IV product over the region, and challenges in handling isolated convection. Work toward developing the forthcoming IPHEX-QPE 1.2 V2 reference product will focus on correcting low elevation rainfall using information from low elevation disdrometers and from NWP model simulations. Spatial intermittency will be addressed through a modified fractal downscaling methodology conditional on the rain support (i.e. the perimeter) of precipitation clusters in StageIV.

## 1. Introduction

Quantitative Precipitation Estimates (QPE) are essential for all water research and applications. Accurate QPEs capture realistic spatial and temporal variability of rainfall to close the water budget at desired catchment scales is the golden target. However, this is a difficult challenge because of the lack of high resolution accurate precipitation observations be it using point measurements (e.g. raingauges and disdrometers) or spatial measurements (e.g. radars). In mountainous regions, remoteness and difficult access compound the problem for point measurements, whereas terrain blockage artifacts severely constrain the geometry of radar operations, and thus the measurement volume. Indeed, radar-based QPE in regions of complex topography remains inadequate despite continuous efforts to calibrate and improve radar products using more sophisticated approaches (e.g. Zhang et al. 2014).

This report describes the methodology used to develop Version 1 of the reference rainfall product for the core region of the Integrated Precipitation and Hydrology Experiment (IPHEx, Barros et al. 2014), that is centered in the Pigeon River Basin in North Carolina (Fig.1). The IPHEx-QPE-1.1 V1 is a 10-year combined raingauge-radar dataset of hourly rainfall at 1 km<sup>2</sup> resolution. Because most of the raingauge observations used for the product are at high elevations, a Version 2 is being developed with low elevation disdrometer data. Finally, development of Version 3 is ongoing that will be constrained to close the water budget at event, season and annual time-scales.

Radar-based QPE is significantly influenced by systematic errors because of retrieval algorithms, measurement limitations, and hardware calibration (Anagnostou et al., 2001; Borga and Tonelli, 2000; Fulton et al., 1998; Nelson et al., 2010; Prat and Barros, 2010b; Steiner et al., 1999; Villarini and Krajewski, 2010). Optimally merging raingauge measurement and radar observations via bias correction methods and kriging-based methods has been widely used in the development of high resolution QPE data sets (Tao and Barros, 2013; Sideris et al., 2014; Seo and Breidenbach, 2002; Seo et al., 1990; Gabella et al., 2000; Krajewski and Georgakakos, 1987). In deriving the reference product for IFloodS (Iowa Flood Studies), Seo et al. (2018) first evaluated the error structure of various radar rainfall products against raingauges, and they found that radar-only rainfall QPE was significantly inferior to combined radar-rainfall QPE products, and in particular StageIV (Lin and Mitchell, 2005). To achieve the reference product, they subsequently fitted error models to address systematic errors (overall and conditional bias), and then combined various products optimally to minimize overall random error features. One important contribution of the IFloodS work is the fingerprinting of the idiosyncrasies of different radar retrieval algorithms across scales and rainfall regimes which result in rainfall products that underperform against operational raingauge-only interpolation algorithms where there is an adequate density of gauges. One complication is the fact that radar measurement errors can be highly non-stationary in space and time which explains the limited improvement obtained from global error models as noted by Seo et al. (2018). In mountainous regions, this problem can be expected be further amplified due to interactions among weather regimes, precipitation systems and topography.

The unique advantage of radar measurements among precipitation measurement systems is their space-filling nature from which spatial fields of rainfall can be derived. The limitation is two-fold: 1) it is an indirect measurement and retrieval algorithms are necessary to convert reflectivity radar to quantitative precipitation estimates; and 2) the spatial resolution depends on the control volume of measurement over which the reflectivity is integrated. The latter is addressed

here via downscaling to achieve the desired resolution. While extensive studies have been done over the past decades, stochastic downscaling of rainfall fields remains an open problem (Bindlish and Barros, 2000; Kim and Barros, 2001; Rebora et al., 2006; Barros and Tao, 2008; Tao and Barros 2010; Nogueira and Barros, 2015). Bindlish and Barros (2000) introduced wind redistribution modulated by terrain into the fractal downscaling/upscaling framework proposed by Bindlish and Barros (1996) to incorporate orographic enhancements effects while preserving the spatial statistics across scales and capturing the temporal evolution of scaling behavior. However, these modifications require high resolution time-varying wind data. To overcome this problem, Rebora et al. (2006) established a rainfall downscaling technique which is similar to Bindlish and Barros (1996), assuming the scaling behavior of rainfall fields is the same over a time interval. Albeit limited by the original coarse resolution information available, fractal downscaling methods are based on the assumption of spatial self-similarity, and the statistical properties of fields at coarse scales are preserved in the downscaling process in contrast with other interpolation methods, and no calibration or optimization is required (Tao and Barros, 2010; Nogueira and Barros, 2015). Moreover, fractal downscaling methods are inherently stochastic, the outcome of the downscaling process itself is a distribution or ensemble of rainfall fields, and thus no extra work is necessary to characterize product uncertainty.

For developing the IPHEX reference rainfall, that is the *IPHEX-QPE-1.1 V1* reference quantitative precipitation estimation (*RQPE*) product, we start with the Stage IV combined radar-rainfall product (hourly,  $16\text{km}^2$ ) as the baseline spatial support. Subsequently, hourly Stage IV fields are downscaled to  $1\text{km}^2$ , and for each hour conditional bias correction and linear kriging algorithms are applied to derive an unbiased rainfall field at hourly, seasonal and inter-annual scales at the raingauge locations that compose the core IPHEX raingauge network (Barros et al. 2017). The reference IPHEX product represents a significant improvement over Stage IV and over MRMS (Zhang et al. 2014) over the region of study. Nevertheless, independent evaluation against disdrometer observations during IPHEX shows that the reference product overestimates rainfall at low elevations and on the lee side of individual ridges that is different from event to event depending on the weather system.

The present report is organized as follows. Data are described in Section 2. Section 3 presents methods and evaluation metrics. Overall evaluation and results of error analysis of the *IPHEX-QPE-1.1 V1* RQPE 10-year data set product are presented in Section 4, followed by conclusion in Section 5.

## 2. Data

### 2.1 IPHEX Raingauge Observations

A high resolution raingauge network has been in operation in the Southern Appalachian Mountains since 2007 in support of NASA's Precipitation Measurement Missions (PMM) program ground validation (GV) activities (Prat and Barros, 2010a). Although the total number of gauges in the network has changed over time, a baseline network with a minimum of 34 raingauges has been maintained in the Pigeon River basin, over the ten-year reference period 2007-2018 before, during and immediately after IPHEX. A map of the baseline raingauge network with individual gauges identified by numbers is shown in Figure 1, whereas detailed geographical coordinates of the gauges are listed in Table 1. Typical raingauge measurement errors include

deposition of dust or foreign materials on the funnel surface that affect its wetting properties, and clogging of the piping and mesh filters, that can occur in-between maintenance visits, wind effects, and representativeness errors related to the location and density of the network proper. Turbulence that develops under strong wind conditions decreases the number of raindrops that are captured by the gauge resulting in underestimation errors on the order of 2-18% (e.g. Wang and Wolff, 2010). The raingauge network is visited at least thrice per year and careful maintenance is conducted including cleaning of raingauges and their surroundings, and on-site calibration to maintain operational errors below 3%. Although it is difficult to identify and correct wind artifacts, the rigorous maintenance protocol provides assurance of the quality of the raingauge measurements overall. Locations with strong winds in the IPHEX domain are not within the region selected for developing the reference product, albeit such instances may occur. In this work, we use these hourly rainfall measurements to adjust radar-based QPE. In-situ rain-gauge data are publicly and available and can be found at <http://dx.doi.org/10.5067/GPMGV/IPHEX/GAUGES/DATA301>.

In addition to the raingauges, a network of Parsivel disdrometers was deployed during the IPHEX EOP (Extended Observing Period, 2013-2014) which was augmented during the IOP (Intense Observing Period, 5/1/2014-6/15/2014). Disdrometer locations are identified by the letter P in Figure 1. Due to the limited duration of the disdrometer measurements, the disdrometer data were used only independent evaluation of V1 of the reference product. One important difference between the raingauge and the disdrometer locations is that the raingauges are generally placed on ridges, whereas most disdrometers are placed on hillslopes in the inner region or at low elevations. This is a crucial difference the implications of which will be discussed in detail in Section 4.

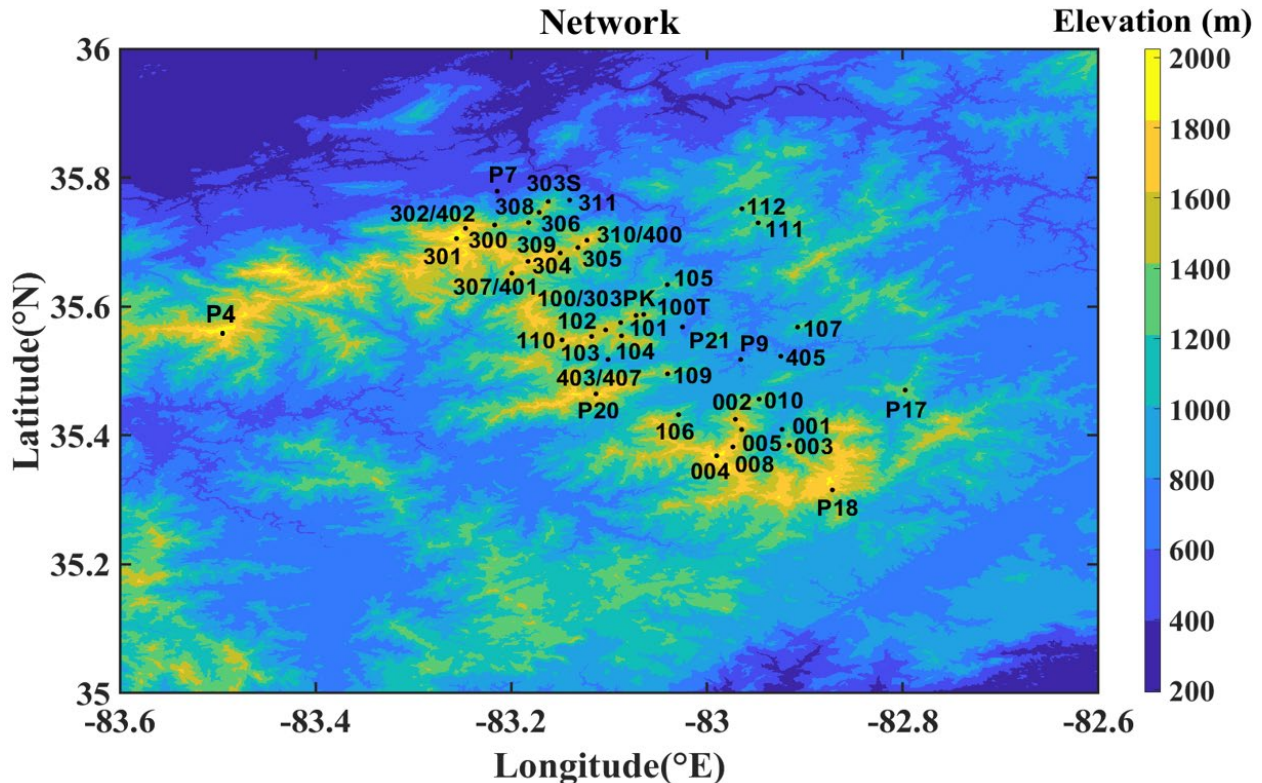


**Figure 1** - Map of ground based observations. Locations marked by numbers only are raingauges; locations marked by numbers preceded by P are disdrometers. See Table 1 for list of stations and geographical coordinates.

**Table 1** – Index, and coordinates for the raingauge stations marked in Figure1. The index is used to identify specific gauges in some of the graphs. Two raingauges at Purchase Knob a supersite in the inner mountain region are highlighted in bold font. Shaded rows indicate stations with collocated raingauges that have different temporal resolution (e.g. tip size).

NO.	SITE ID.	Lat.	Lon.	Elev. (m)
1	RG001	35.39830	-82.91300	1156
2	RG002	35.41750	-82.97140	1731
3	RG003	35.38460	-82.91610	1609
4	RG004	35.36830	-82.99020	1922
5	RG005	35.40890	-82.96460	1520
6	RG008	35.38210	-82.97360	1737
7	RG010	35.45640	-82.94680	1478
8	RG100	35.58610	-83.07250	1495
9	RG100T	35.58767	-83.06468	1485
10	RG101	35.57500	-83.08820	1520
11	RG102	35.56370	-83.10360	1635
12	RG103	35.55340	-83.11790	1688
13	RG104	35.55490	-83.08800	1584
14	RG106	35.43210	-83.02910	1210
15	RG109	35.49560	-83.04040	1500
16	RG110	35.54810	-83.14820	1563
17	RG300	35.72653	-83.21692	1558
18	RG301	35.70552	-83.25595	2003
19	RG302	35.72135	-83.24675	1860
<b>20</b>	<b>RG303PK</b>	<b>35.58610</b>	<b>-83.07253</b>	<b>1495</b>
<b>21</b>	<b>RG303S</b>	<b>35.76295</b>	<b>-83.16222</b>	<b>1490</b>
22	RG304	35.67010	-83.18287	1820
23	RG305	35.69150	-83.13190	1630
24	RG306	35.74597	-83.17148	1536
25	RG307	35.65163	-83.19952	1624
26	RG308	35.73027	-83.18237	1471
27	RG309	35.68297	-83.15003	1604
28	RG310	35.70273	-83.12263	1756
29	RG311	35.76507	-83.14042	1036
30	RG400	35.70273	-83.12263	1756
31	RG401	35.65163	-83.19952	1624
32	RG402	35.72135	-83.24675	1860
33	RG403	35.51777	-83.10113	925
34	RG407	35.51777	-83.10113	925

### 2.3 Radar Data

The NCEP/EMC (Environmental Modeling Center) Stage IV is a QPE product from the National Weather Service (NWS) derived from the regional hourly and 6-hourly multisensor (radar + NWS raingauges) precipitation analyses (MPAs), which is further improved with new

analyses from River Forecast Centers (RFCs) over the conterminous United States (CONUS) (Lin and Mitchell, 2005). Due to ground clutter effects and uncertainty in retrieval algorithms, Stage IV data sets have significant biases and errors in rainfall detection in mountainous regions as stated earlier. In this study, the PMM GV raingauge observations from the Southern Appalachians are used to correct StageIV. We also have limited access to hourly Multiresolution Multisensor (MRMS) combined radar and raingauges QPE at 1 km<sup>2</sup> (Zhang et al. 2014) during the IPHEX IOP (Intense Observing period) for independent evaluation.

### 3. Methods

The framework adopted for deriving the IPHEX reference product V1 is summarized in Figure 2.

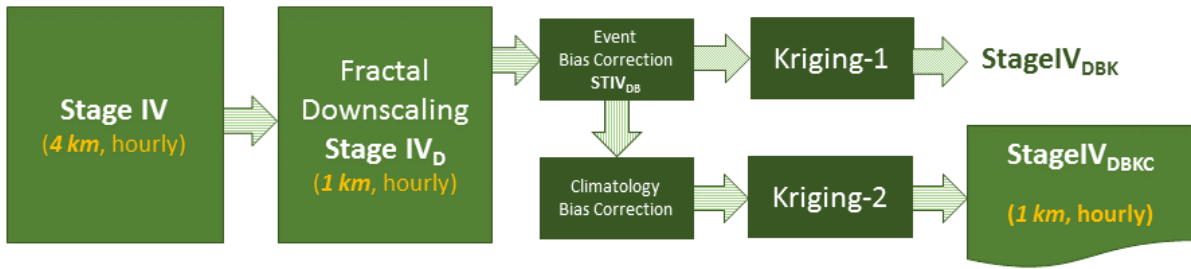


**Figure 2 – Workflow to generate the IPHEX reference product V1.**

First, fractal downscaling was used to generate high resolution hourly StageIV<sub>D</sub> at 1km from the original Stage IV product. Downscaling to 250m resolution was also conducted for modeling applications. Although the 250 m product was not stored as part of the reference product, it can be generated at any time if needed. After downscaling, bias correction and ordinary kriging were applied consecutively to modify the downscaled StageIV<sub>D</sub> to StageIV<sub>DBK</sub> at hourly time-scale. The StageIV<sub>DBK</sub> data were subsequently evaluated against the raingauge climatology from 2008 to 2017, and a climatology corrected version StageIV<sub>DBKC</sub> was obtained to correct systematic radar measurement errors conditional on rainfall regime.

#### 3.1 Fractal downscaling

In this study, we aim to derive high resolution QPE data sets from original Stage IV using fractal downscaling. Under the assumption of self-similarity, the Hurst coefficient  $H$ , fractal dimension  $D$ , and the spectral exponent  $\beta$  are related as follows:

$$D = \frac{7-\beta}{2} \quad (1)$$

$$H = \frac{\beta-1}{2} \quad (2)$$

The parameter  $\beta$  describes the distribution of the rainfall at different scales, and it is estimated as the slope of the 2D Fourier spectrum of the rainfall field (log-log plot). The power spectral density  $Z(u,v)$  in the 2D Fourier domain describing the relationship between spatial scale and rainfall is :

$$Z(u,v) = \left(\frac{L}{N}\right)^2 \sum_{x=0}^{N-1} \sum_{y=0}^{N-1} z(x,y) \exp\left[-\frac{2\pi i}{N}(ux + vy)\right] \quad (3)$$

where  $u$  and  $v$  represent the transform of  $x$  and  $y$  in Fourier domain,  $N$  is the total number of grid points in each direction. Additionally, the spectral density at wavenumber  $k = 1.0$  is defined as the roughness factor, that is the variance of the field. The Hurst coefficient describes the auto correlation strength (range from 0 to 1) with higher values of  $H$  implying higher auto-correlation, that is persistence. The mean power spectral density in 2-D Fourier domain is as follows:

$$S_j = \frac{1}{L^2 N_j} \sum_1^{N_j} |Z(u, v)|^2 \quad (4)$$

where  $N_j$  is the number of coefficients that satisfy the condition  $j < \sqrt{u^2 + v^2} < j + 1$ . The mean power spectral density has a power-law relationship with wave number  $k$ , and  $k$  is defined as below:

$$k = \frac{2\pi}{\sqrt{u^2 + v^2}} \quad (5)$$

$$S \sim k^{-\beta-1} \quad (6)$$

where  $\beta$  is the spectral exponent that is the slope of hourly power density spectrum. Assuming the rainfall fields are self-similar, then the information at fine resolutions can be derived from the information at coarser resolution. This is accomplished using a Brownian surface ( $Z_b$ ,  $H=0.5$ ) at the desired fine resolution as spatial support for the interpolation, which is modified in the Fourier domain ( $Z_D$ ) to replicate the distribution of energy slope of the spectral slope and roughness factor per Bindlish and Barros (1996):

$$Z_D(u, v) = \frac{Z_b(u, v)}{k_r^{(\beta-\beta_b)/2}} \exp \left[ \frac{1}{2} \left( S_{r,1} - \frac{\beta+1}{\beta_b+1} S_{r,2} \right) \right] \quad (7)$$

where  $\beta$ ,  $\beta_b$ ,  $Z(u, v)$  and  $Z_b(u, v)$  are respectively the original rainfall fields spectral exponent, Brownian surface spectral exponent, and Fourier transform of interpolation surface and Brownian surface, respectively;  $k_r$  is the wavenumber;  $S_{r,1}$  and  $S_{r,2}$  are the roughness factor of the original rainfall fields and Brownian surface, and  $Z_D$  is the modified rainfall field at the desired resolution in the Fourier domain. Furthermore, the interpolation surface is not unique due to the non-uniqueness of Brownian surfaces, and thus an ensemble of ND rainfall fields with the same spatial statistics can be generated by generating an ensemble of ND Brownian surfaces. Following Nogueira and Barros (2015), here ND=50 and the correction steps in Figure 2 are applied to the ensemble mean.

### 3.2 Bias correction

*Event-scale* - Collocated hourly raingauge measurements and downscaled Stage IV estimates can be related using linear regression as follows:

$$R_g^t(i_g, j_g) = \kappa R_r^t(i_g, j_g) + \varepsilon \quad (8)$$

where  $R_r$  represent radar measurements,  $R_g$  represent raingauge observations,  $\kappa$  and  $\varepsilon$  are respectively the slope (conditional bias correction) and the intercept (systematic bias correction). For each hour, collocated pairs of StageIV<sub>D</sub> estimates and raingauge observations within a radius of  $L = 5$  km centered on the StageIV<sub>D</sub> pixel were identified as long as more than two raingauges measure rainfall different from zero. In the first phase of regional least-square linear regression was applied subsequently to all StageIV<sub>D</sub> pixels. Assuming homoscedasticity, bias correction was

applied only to the StageIV<sub>D</sub> pixel estimates within  $\pm 1-\sigma$  deviation of the regional regression line at hourly time-scale.

*Climatology* - The second phase of bias correction aimed eliminating the systematic bias identified by comparing the diurnal and seasonal cycles against the 10-year gauge climatology that show how radar measurement geometry results in systematic detection errors depending on rainfall regime, thus varying with time-of-day and season. Specifically, this relates to missing shallow rainfall due to overshooting errors in the Southern Appalachian (e.g. Wilson and Barros, 2014; Duan and Barros, 2017; Arulraj and Barros, 2017). For this purpose, the following corrections were added for rainfall below and above a threshold X, where X=2mm/hr in the Pigeon River Basin. When raingauge measurements are less than 2mm/hr and Stage IV<sub>D</sub> estimates are nil, the StageIV<sub>D</sub> value was replaced by the raingauge observations, here termed Light Rainfall Correction (LRC). Furthermore, for each hour, nil StageIV<sub>D</sub> estimates where raingauge measurements are greater than X=2mm/hr were identified and replaced by the mean of the corresponding collocated raingauge measurements, hereafter Mean Rainfall Correction (MRC). Finally, for localized precipitation (i.e. only two rainguages or fewer detect rainfall) normally associated with isolated convective activity, the anomalies calculated as the differences between the STIV<sub>D</sub> obtained from for each pixel and the local raingauge measurements were linearly distributed among the surrounding 25 pixels (5 pixel window centered at the StageIV<sub>B</sub> pixel)– Convective Rainfall Correction (CRC). When more than 2 rainguages measured rainfall, then the anomalies for each pixel were spatially distributed using ordinary kriging as described below – Global Rainfall Correction (GRC).

### 3.3 Ordinary kriging

The Ordinary kriging (OK) estimator is a weighted linear unbiased estimator that predicts (interpolates) values of a variable at a specific location using weights based on the spatial covariance structure of the variable assuming an unknown constant mean value and minimizing prediction variance. In our case, the rainfall differences among raingauge measurements and StageIV<sub>DB</sub> at all raingauge locations were calculated and denoted as  $G(x_i)$  at gauge location i. To generalize the interpolation to any location within a domain of interest, a continuous model to describe the covariance structure of the data is necessary. A commonly used semi-variogram model is the spherical model, which exhibits linear behavior at the origin. A review of different types of semivariogram models can be found in Li and Heap (2008). Mirko Mälicke (et al., 2018) analyzed in detail the differences of several commonly used semivariogram models. They point out that, given the same variogram parameters (nugget, sill and range), spherical models reach to the maximum for comparatively shorter spatial lags (see Figure 1 in Mirko Mälicke et al., 2018), and thus are suitable to capture strong spatial dependencies over short distances as in the case of orographic precipitation (see also McBratney and Webster, 1986, for detailed description of spherical model):

$$\gamma(h) = C_0 + (C - C_0) \left( \frac{3h}{2d} - \frac{1}{2} \left( \frac{h}{d} \right)^3 \right) \text{ if } 0 \leq h \leq d \quad (9.1)$$

$$= C \quad \text{if } h > d \quad (9.2)$$

$$\gamma_{0i} = \frac{1}{N_A} \sum_{k=1}^{N_A} \gamma_{ki} \quad (9.3)$$

$$\gamma_{00} = \frac{1}{N_A} \sum_{k=1}^{N_A} \sum_{l=1}^{N_A} \gamma_{kl} \quad (9.4)$$

where  $d$  is the range,  $h$  is the lag,  $N_A$  is the number of available gauge locations,  $C$  and  $C_0$  are the sill and nugget values. Neglecting local variability and measurement error at the spatial scale of the downscaled radar and raingauge (point) measurements, the nugget is constant and equal to zero (Diggle & Ribeiro, 2007). The rainfall difference at a target point  $x_0$   $Z_{ok}^*(x_0)$  is calculated using a weighted linear combination of all available differences with constraints of unbiased estimator

$$Z_{ok}^*(x_0) = \sum_{i=1}^n \lambda_i^{ok} G(x_i) \quad (10.1)$$

$$\sum_{i=1}^n \lambda_i^{ok} = 1 \quad (10.2)$$

Optimal weights can be obtained by solving following equation by employing Lagrange multiplier  $\mu$ :

$$\begin{pmatrix} \gamma_{11} & \dots & \gamma_{n1} & 1 \\ \vdots & \ddots & \vdots & \vdots \\ \gamma_{1n} & \dots & \gamma_{nn} & 1 \\ 1 & \dots & 1 & 0 \end{pmatrix} \begin{pmatrix} \lambda_1^{OK} \\ \vdots \\ \lambda_n^{OK} \\ \mu \end{pmatrix} = \begin{pmatrix} \gamma_{01} \\ \vdots \\ \gamma_{0n} \\ 1 \end{pmatrix} \quad (11)$$

In this study, OK distributes spatially the differences between available raingauge measurements and radar data, which helps to generate modified radar rainfall fields.

### 3.4 Evaluation Metrics

Standard performance metrics (McBride and Ebert 2000; Wang, 2014) including false alarm rate (FR), probability of detection (PD), threat score (TS), and Heidke skill score (HSS), as well as bias, and the root-mean-square error (RMSE) are used to evaluate the corrected downscaled hourly rainfall. An instance when both radar product and the observations O used for evaluation exceed a specified rain rate threshold is a hit (H); when the opposite happens, the estimate is classified as a miss (M) if the observation matches the criterion, and a false alarm (FA) otherwise. The performance metrics are determined by combination of Hs, Ms and FAs:

$$Bias = \frac{1}{N} \sum_{n=1}^N (O_n - R_n) \quad (12)$$

$$RMSE = \sqrt{\frac{1}{N} \sum_{n=1}^N (O_n - R_n)^2} \quad (13)$$

$$FR = \frac{FA}{H+FA}, 0 \leq FR \leq 1 \quad (14)$$

$$PD = \frac{H}{H+M}, 0 \leq PD \leq 1 \quad (15)$$

$$TS = \frac{H}{H+FA+M}, 0 \leq TS \leq 1 \quad (16)$$

$$HSS = 2 * \frac{Z*H-FA*M}{((H+FA)*(Z+FA)) + ((M+H)*(M+Z))}, -1 \leq HSS \leq 1 \quad (17)$$

where Z is the overall number of zeros (when neither radar data nor raingauge measurements match the threshold criterion). A TS of 0.5 implies that the criterion is satisfied at least 50% of the time,

and a higher value is indicative of superior performance. A TS=0.33 is indicative of performance similar to persistence, meaning predicted values in the next hour are the same as values at the previous hour. HSS describes the fractional improvement of the corrected IPHEx estimates over StageIV. Since HSS is a normalized score, it facilitates comparison among different data sets. An HSS of 0 means that the performance is not better than random chance. Note that we use all raingauges in the development of the reference rainfall (RR) and therefore evaluation against the raingauges serves to verify whether the two-step correction consisting of two unbiased estimators (linear bias correction + detection climatology and ordinary kriging) is also an unbiased estimator, and whether detection statistics and thus characterization of spatial intermittency improves.

### 3.5 Error Modeling

Error modeling in this study targets three major sources of uncertainty: 1) StageIV downscaling; 2) bias correction; and 3) Kriging. Errors specific to the radar algorithm errors and spatial mapping are not explicitly accounted although they are present implicitly in the original StageIV and therefore are propagated through the correction process.

#### 3.5.1 Downscaling

In the fractal downscaling part, spatial scaling of statistical scale invariant fields can be described by investigating their statistical moments. Lavalée (et al., 1993) suggested a generic multiscaling relation:

$$M_q = \langle \varphi_\lambda^q \rangle \approx \lambda^{K(q)} \quad (17)$$

Where  $\langle \rangle$  represents statistical expectation,  $\varphi$  is a conserved statistic on average from scale to scale.  $q$  is the moment order, and  $\lambda = L_0/l$  is the scale ratio.  $L_0$  is the largest scale in the domain and  $l$  is the domain resolution. For a multifractal quantity the moment scaling exponent function,  $K(q)$  is a convex nonlinear function of  $q$  and therefore infinite number of scaling exponents are necessary to fully characterize the scaling behavior. Based on the stability properties of cascade generators, Schertzer and Lovejoy (1987) showed that  $K(q)$  can be modeled by:

$$K(q) = \begin{cases} \frac{C_1}{\alpha-1} (q^\alpha - q), & \alpha \neq 1 \\ C_1 q \log(q), & \alpha = 1 \end{cases} \quad (18)$$

The levy index,  $\alpha$ , is in the range [0, 2], and it describes the degree of multifractality, with  $\alpha = 0$  for monofractals. The codimension of the mean singularity,  $C_1$ , describes the intermittency of the mean process such that the higher  $C_1$ , the more intermittent the field, and the more sparse the spikes of high values (Sun and Barros, 2010).

Besides  $\alpha$  and  $C_1$ , it is necessary to estimate another parameter describing the maximum order of singularity  $\gamma_s$ , which indicates the amplitude of the fluctuations of rainfall extremes. The statistical meaning of this parameter is the upper limit of the observed singularity in a finite data set. Regarding time series, it can be calculated (Hubert et al. 1993):

$$\gamma_s = \gamma_0 \left[ 1 - \alpha \left( \frac{C_1}{D} \right)^{-1/\alpha'} \right] \quad (19)$$

Where  $\alpha'$  satisfies  $\left(\frac{1}{\alpha}\right) + \left(\frac{1}{\alpha'}\right) = 1$ .  $\gamma_0 = C_1/(1 - \alpha)$  is the maximum order of singularity for an infinite length of time series.  $\gamma_s$  depends on both  $\alpha$  and  $C_1$ .

A detailed description of calculating  $\alpha$  and  $C_1$  using Double trace moment (DTM; Lavallee et al. 1991b) can be found in the previous papers (e.g Sun and Barros, 2010). After the determination of all three parameters, assuming each pixel in our data fields is a station, one can obtain a map for each of these three parameters. Following Sun and Barros (2010), rainfall distribution can then be simulated using these parameters and rainfall spatial patterns and uncertainties can be analyzed.

Spectral analyses can also be used in this part to describe the scale-invariant behavior:

$$E(k) \sim k^{-\beta-1} \quad (20)$$

And uncertainties exist in generating interpolating surfaces:

$$Z_D(u, v) = \frac{z_b(u, v)}{k_r^{(\beta-\beta_b)/2}} \exp \left[ \frac{1}{2} \left( S_{r,1} - \frac{\beta+1}{\beta_b+1} S_{r,2} \right) \right] \quad (21)$$

Where all components are explained in Eqn. 7.

Following Nogueira and Barros (2015), we used least squares to determine spectral exponent of the original rainfall fields, assuming the residuals of rainfall fields in a log-log Fourier domain are following a Gaussian distribution that corresponds to a log-normal distribution in Euclidean space. Stochastic errors are introduced in this process as well as in the determination of roughness factors. These errors are propagated through transformation equation 18 into interpolation surfaces, leading to errors in replicates of downscaling products.

### 3.5.2 Bias Correction

In the linear bias correction part, the error is characterized by the following equation, and the coefficients are determined using least squares minimization:

$$R_g^t(i_g, j_g) = \kappa R_r^t(i_g, j_g) + \varepsilon \quad (22)$$

where the subscripts  $r$  and  $g$  refer to the gauges and the radar-based pixel, respectively. Likewise, the corrected  $R_*^t$  of the pixel values where gauges exist is implemented as follows:

$$R_*^t(i_g, j_g) = \kappa R_r^t(i_g, j_g) + \varepsilon \quad (23)$$

Since  $\kappa$  and  $\varepsilon$  are determined by least squares,  $\varepsilon$  can be interpreted as stochastic error and  $\kappa$  can be interpreted as an overall bias factor. This linear relationship is specifically dependent on each event, that is on an hourly basis. Assuming  $\varepsilon$  satisfies a normal distribution with mean equal to zero  $\varepsilon \sim N(0, \sigma)$ , the mean square error (MSE) then can be expressed as:

$$\begin{aligned} MSE &= \text{Var}(R_g^t(i_g, j_g) - R_*^t(i_g, j_g)) = E[(R_g^t(i_g, j_g) - (\kappa R_r^t(i_g, j_g) + \varepsilon))^2] \\ &= E[(\kappa R_r^t(i_g, j_g))^2] + E[(R_g^t(i_g, j_g))^2] + E(2\varepsilon\kappa R_r^t(i_g, j_g)) - E(2\varepsilon R_g^t(i_g, j_g)) - \\ &\quad E(2\kappa R_r^t(i_g, j_g)R_g^t(i_g, j_g)) + E(\varepsilon^2) \end{aligned} \quad (24)$$

Assuming  $\varepsilon$  is independent of the radar retrieval algorithm, and assuming a simple<sup>1</sup> StageIV estimation error that relates the error to the magnitude of the estimate proper by a linear factor  $\alpha \geq 0$  conditional on rainfall regime  $R_{r,c}^t$ , Eq. (24) can be further simplified:

$$MSE = \alpha(R_{r,c}^t) E[(R_r^t(i_g, j_g))^2] + E(\varepsilon^2) + E[(R_g^t(i_g, j_g))^2] + E(2\kappa R_r^t(i_g, j_g) R_g^t(i_g, j_g)) \quad (25)$$

For the second term of Eq. 25,  $\varepsilon^2$  satisfies a  $\chi^2$  distribution (Chi Square distribution) with mean greater than 0.

### 3.5.3 Kriging

The ordinary kriging estimator minimizes the variance of the error assuming the mean  $\tau$  is constant and unknown:

$$E(G(x_0)) = \tau \quad (25)$$

$$Var(x_0) = E[(G(x_0) - Z_{ok}^*(x_0))^2] \quad (26)$$

Rewriting Eqn. 11 in matrix notation:

$$\boldsymbol{\gamma}\boldsymbol{\lambda} = \mathbf{D} \quad (27)$$

The variance of the prediction at location  $x_0$  can be estimated following Bailey and Gatrell (1995):

$$\begin{aligned} \sigma_{ok}^2(x_0) &= MSE = Var(x_0) = Var(G(x_0)) + Var(Z_{ok}^*(x_0)) - 2Cov(Z_{ok}^*(x_0), G(x_0)) \\ &= \sigma^2(x_0) + Var(\sum_{i=1}^n \lambda_i^{ok} G(x_i)) - 2Cov(Z_{ok}^*(x_0), G(x_0)) \\ &= \sigma^2(x_0) + \sum_{i=1}^n \sum_{j=1}^n \lambda_i^{ok} \lambda_j^{ok} \gamma_{ij} - 2 \sum_{j=1}^n \lambda_j^{ok} \gamma_{j0} \\ &= \sigma^2 - \boldsymbol{\gamma}' \mathbf{D} \end{aligned} \quad (28)$$

A spherical semivariogram model can be used to distribute the point estimates  $\sigma_{ok}^2(x_0)$  as described in Section 3.3.

## 4. IPHEx RQPE Evaluation and Discussion

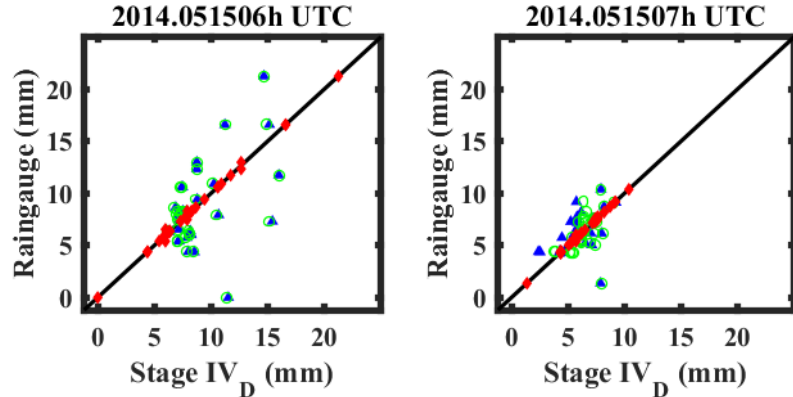
### 4.1 Event-Scale Evaluation

Event-scale evaluation of StageIV<sub>DBK</sub> is presented for comparisons against raingauge measurements in the IPHEx domain during the IOP (2014-05-01 to 2014-06-15). The most intense rainfall across the Pigeon River Basin was observed during the passage of a frontal system on May 15<sup>th</sup>, 2014, and thus hourly-scale evaluation metrics are presented for this event<sup>2</sup>.

---

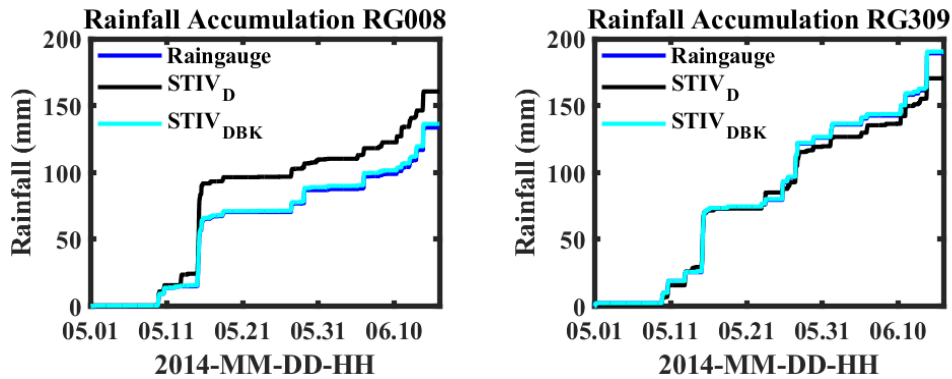
<sup>1</sup> If available, the NEXRAD-StageIV estimation error model should be used instead.

<sup>2</sup> Hourly rainfall fields at hour YY represent the accumulation of rainfall during the previous hour.



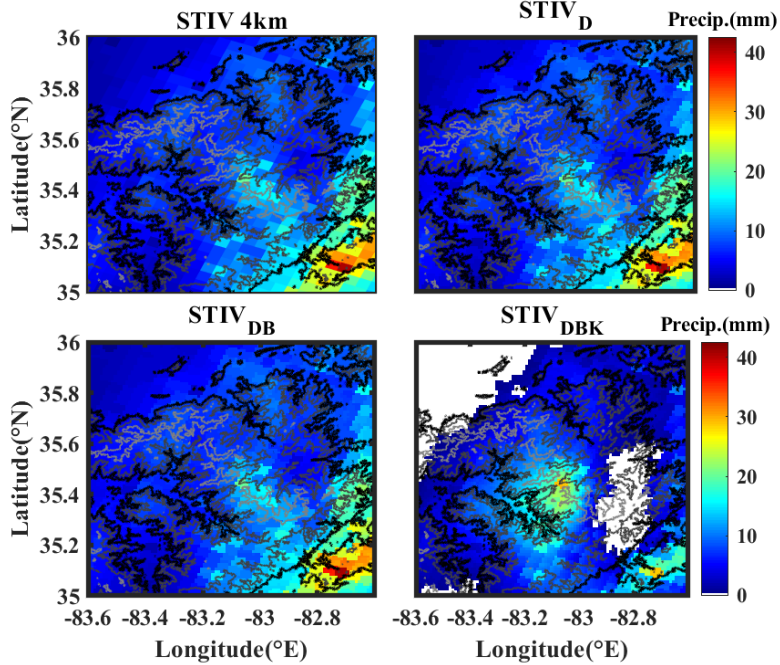
**Figure 3** - Raingauge data compared against StageIV<sub>D</sub> (blue triangles, downscaled Stage IV) data and corrected StageIV<sub>D</sub> (green circles are StageIV<sub>DB</sub>, and red diamonds are StageIV<sub>DBK</sub>).

Figure 3 shows that bias correction alone does not significantly impact the rainfall at 06 UTC (left panel) due to the high spatial variability of rainfall and high rainfall amounts within the domain suggesting that the homoscedasticity assumption is inadequate for this field. Bias correction is effective for the more moderate and less spatially variable rainfall at 07UTC (right panel). In both cases, the most significant improvement is the outcome from OK resulting in unbiased rainfall fields. Cumulative rainfall curves during the IPHEX IOP at two selected raingauge locations (see Figure 1) on the eastern (left panel) and western ridges (right panel) ridges are shown in Figure 4 (see Figure 1).



**Figure 4** - Cumulative rainfall curves at selected raingauges (see Figure 1 for location) during the IPHEX IOP.

The spatial rainfall fields at 07 UTC are shown in Figure 5 including the original StageIV field at 4km resolution, the downscaled StageIV<sub>D</sub> at 1 km resolution, and StageIV<sub>DB</sub> and StageIV<sub>DBK</sub> respectively after bias correction and after OK. Note the significant enhancement of precipitation in the inner mountain region between 83.2-83.0 W and reduction of precipitation elsewhere.



**Figure 5** - Spatial rainfall fields on 2014-05-15, 06-07 UTC.

## 4.2 Climatology Evaluation

Upon generating ten years (2008-2017) of the RQPE fields one hour at a time (StageIV<sub>DBK</sub>), error analysis was conducted at the raingauge locations with a focus on the statistics of the diurnal and seasonal cycles of rainfall (mean and variance):

$$\text{Mean} = \frac{\sum \text{Non zero rainfall of a product (when } RG > 0\text{mm)}}{\# \text{ of Non zero events in } RG \text{ data}} \quad (29)$$

$$\text{Variance} = \text{variance}(\text{Non zero events (when } RG > 0\text{mm)}) \quad (30)$$

Analysis of the diurnal cycle on a seasonal basis reveals bias patterns linked to radar operations, and in particular terrain blockage, radar beam overshooting, and excessive attenuation that may vary from hour to hour but when taken over a long period of time indicate localized errors in space and time that reflect the site hydrometeorology. Light and shallow rainfall is a particular challenge in the region of study (e.g. Duan et al. 2015; Duan and Barros, 2017; Arulraj and Barros, 2017). The peak number of missed rainfall corresponds to about 10-15% of the total number of hours for each season in the late afternoon. The missed events correspond to both light and moderate rainfall, and occasionally to isolated heavy rainfall likely associated with isolated thunderstorms. To improve the climatology, the STIV<sub>D</sub> product was modified applying the series of corrections described in Section 3.2 as illustrated by Figure 6: LRC, MRC, CRC and GRC

The new climatologically corrected STIV<sub>DBKC</sub> fields have significantly accurate diurnal cycle comparing to raingauges. This process is illustrated in Figure 6 for one raingauge in eastern ridges (left panel) and another in the western ridges (right panel).

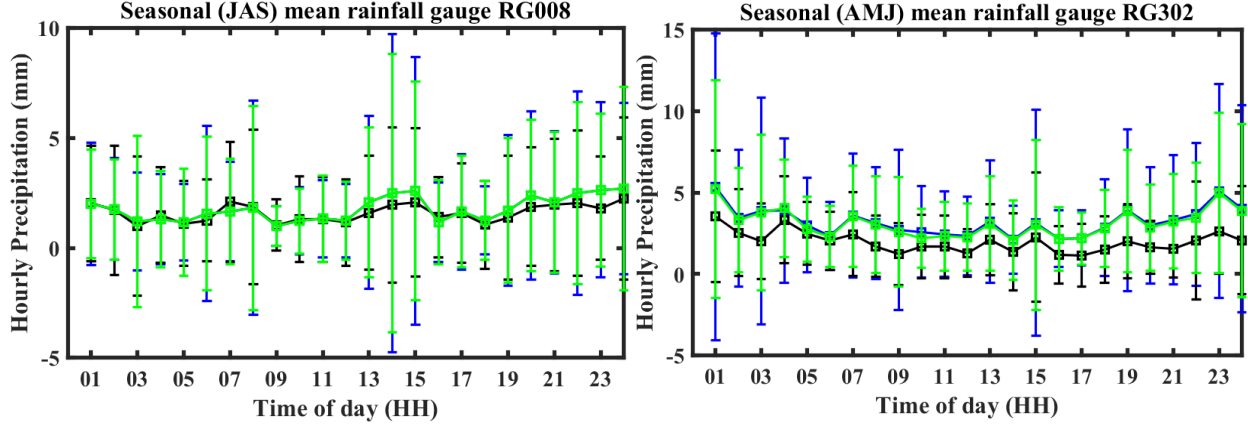


**Figure 6** - Diurnal cycle of rainfall (mean and  $\pm$ standard deviation) for different seasons and gauge locations. Left panel - Summer (JAS: July-August-September) at RG008 in the eastern ridges. Right panel – Spring (AMJ; April-May-June ) at RG302 in the western ridges. Raingauge measurements (blue); StageIV<sub>DBK</sub> (black); StageIV<sub>DBKC</sub> (green).

Biases in original StageIV<sub>D</sub> are more significant over the western ridges (e.g. right panel) at all times of day reflecting the impact of cloud immersion and seeder-feeder enhancement of low level precipitation over the ridges (Duan and Barros, 2017), with mid-day bias being a problem across the region (e.g., Barros and Arulraj, 2019). Overall, analysis of the StageIV<sub>DBKC</sub> fields demonstrates that the climatology corrections work well in terms of mean rainfall. This is also the case with regard to the missed detection errors. Figure 7 shows the diurnal cycle of missed precipitation at two selected gauge locations (top row) in the winter (January-February and March – JFM) in StageIV that are preserved in Stage IV<sub>D</sub> (black) and StageIV<sub>DBK</sub> (cyan). These missed precipitation events correspond to instances of very light rainfall (bottom row) at the raingauge locations ( $< 1.5$  mm/hr). After applying the LRC and MRC climatology corrections, the missed detection problems (cyan) in StageIV<sub>DBK</sub> are largely eliminated for the StageIV<sub>DBKC</sub> fields (green).

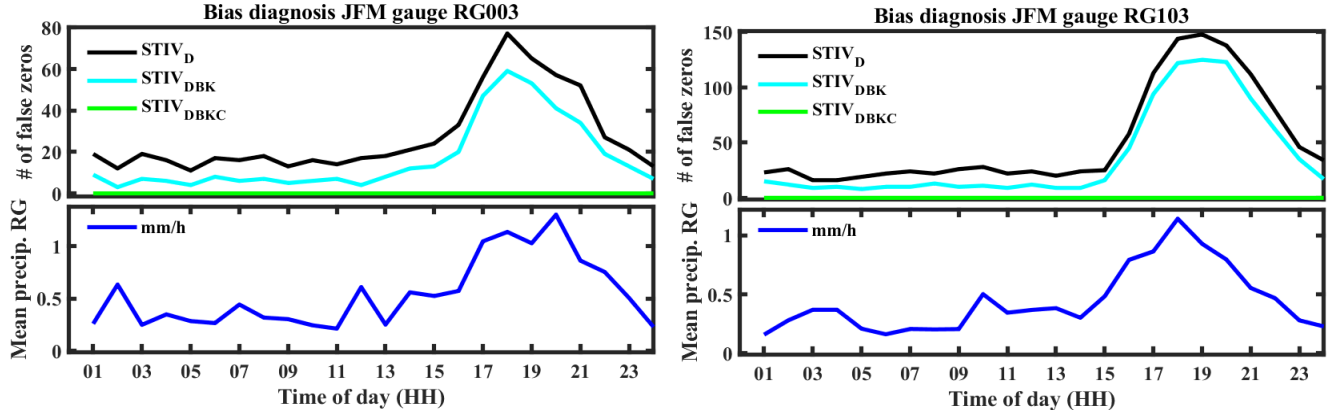


**Figure 7** –Top row - Wintertime (January-February-March, JFM) diurnal cycle of missing precipitation in the eastern ridges (RG003) and in the inner region (RG103) for each of the RR products: . Bottom row- same as top row for the raingauge climatology of hourly rainfall (blue). StageIV<sub>D</sub> (black); StageIV<sub>DBK</sub> (cyan); StageIV<sub>DBKC</sub> (green).

#### 4.3 Performance Metrics

Mean values of the performance metrics (defined in Section 2.4) of hourly downscaled corrected rainfall at the 34 reference raingauge locations during the IPHEX IOP in 2014 are shown in Figure 8 with TS and HSS calculated for rainfall rates  $> 1$ mm/hr. StageIV<sub>DBKC</sub> data sets have

much lower BIAS and RMSE than the downscaled Stage IV with values below 0.1 mm/hr at all times. Note TS and HSS scores consistently > 0.5 for StageIV<sub>DBKC</sub>.

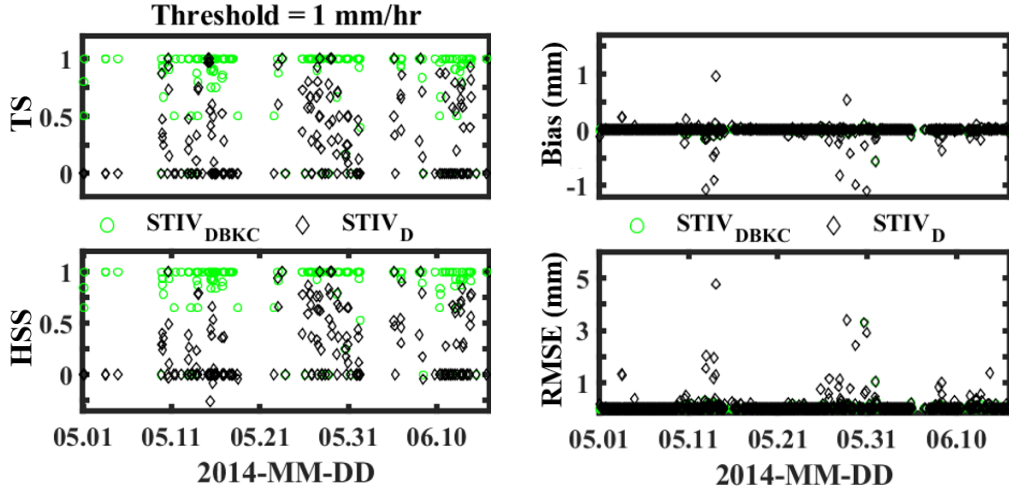


**Figure 8 –** Performance metrics (Section 2.4) of Stage IV<sub>D</sub> (black) and Stage IV<sub>DBKC</sub> (green) during the IPHEX IOP.

When integrated over the ten-year period, the averaged seasonal HSS and TS statistics of STIV<sub>DBKC</sub> demonstrate significantly better performance comparing to STIV<sub>D</sub> for all hours of the day (Figure 9). Moreover, note that there is no decrease in TS trend with increasing precipitation rate threshold (Figure 10) which indicates that the climatology correction is working for the heavy rainfall amounts that tend to be more linked to localized thunderstorm activity as well as for light rainfall. Finally, the average errors of seasonal rainfall accumulation for each raingauge over the 10 year length of record for StageIV<sub>DBKC</sub> were calculated as follows

$$\text{Cumulative errors} = \frac{\sum_{\text{year}=2008}^{\text{year}=2017} \text{STIV}_{\text{season}, \text{DBKC}} - \sum_{\text{year}=2008}^{\text{year}=2017} \text{RG}_{\text{season}}}{\sum_{\text{year}=2008}^{\text{year}=2017} \text{RG}_{\text{season}}} \quad (31)$$

and similarly for Stage IV<sub>D</sub>. Figure 11 shows the diurnal cycle and seasonality distribution of RMSE conditional on rain rate. The RMSE generally stays below 0.1 mm/hr except in the early morning and in the late afternoon in the cold season. In part this error could be related to snowfall which is not properly accounted for as the raingauges are not heated. A synthesis of the cumulative errors of rainfall at all locations is provided in Figure 12 (top row), and for contrast the same analysis is provided for StageIV<sub>D</sub>. Note the seasonal scale errors are mostly in the warm season (AMJ and JAS) and on average remain below 0.5% except at Purchase Knob (indices 20 and 21, Table 1), and over the western regions for stations (30,31,32,33,34) where raingauges with different temporal resolution are collocated. The larger errors are tied with the higher resolution raingauges (i.e. smaller tips), which suggests the errors can be attributed to temporal resolution, that is to say sub-hourly variability in rainfall intensity and consequently rainfall accumulation. Nevertheless, the errors do not exceed 2-3 % in all cases. Thus, overall the performance metrics and error analysis show that the methods are applied correctly and that they are working as they should in terms of integrating the raingauge observations to the downscaled radar product. This does not mean however that the reference product approaches the true rainfall with the same metrics, such as RMSE $\leq$ 0.1mm/hr. Indeed, this will be discussed by error analysis against independent measurements at other locations within the region the study in Section 4.4.

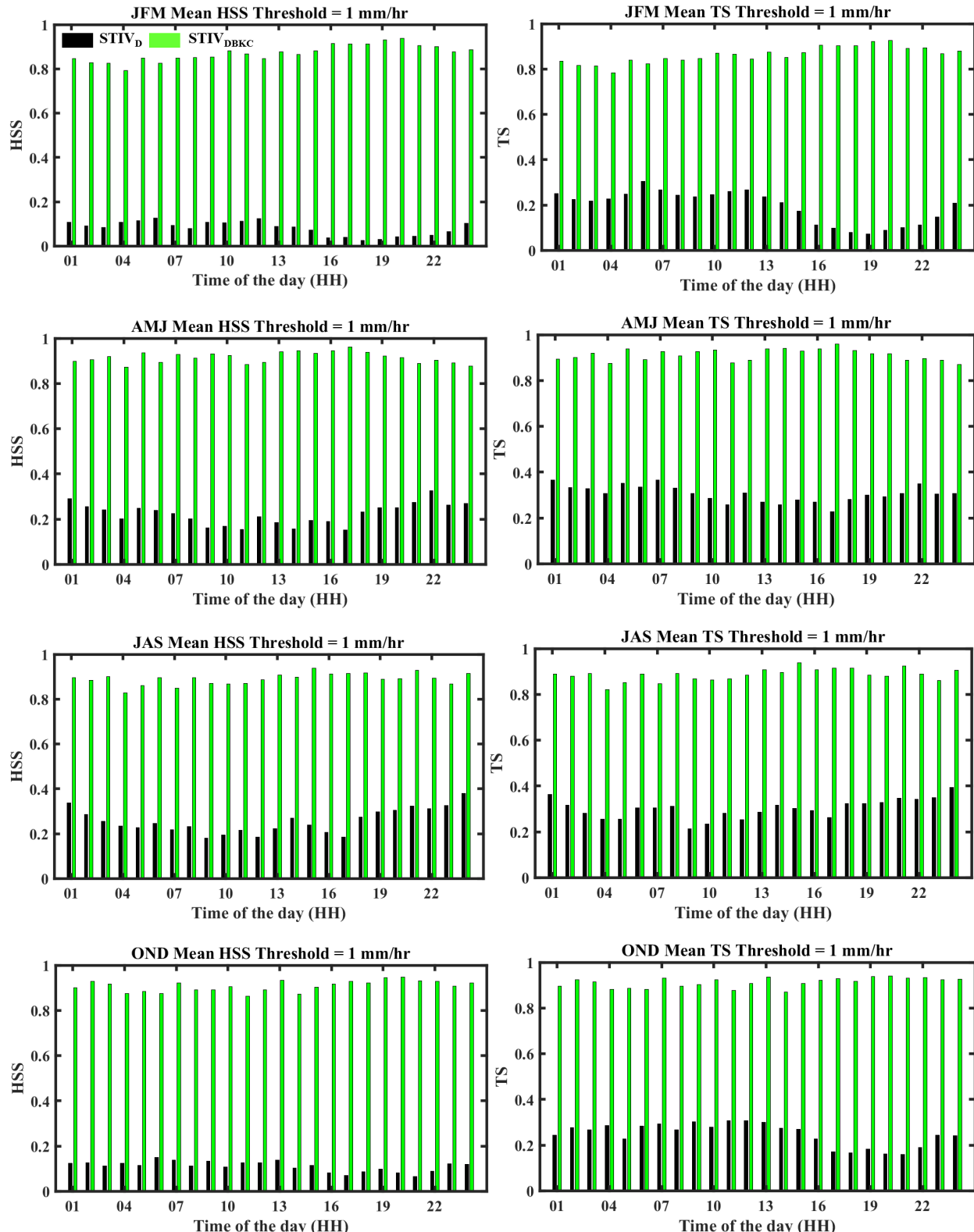


**Figure 9** – Diurnal cycle of mean HSS and TS statistics as a function of season for the entire network over the 10-year reference period (2008-2017). StageIV<sub>D</sub> (black); StageIV<sub>DBKC</sub> (green).

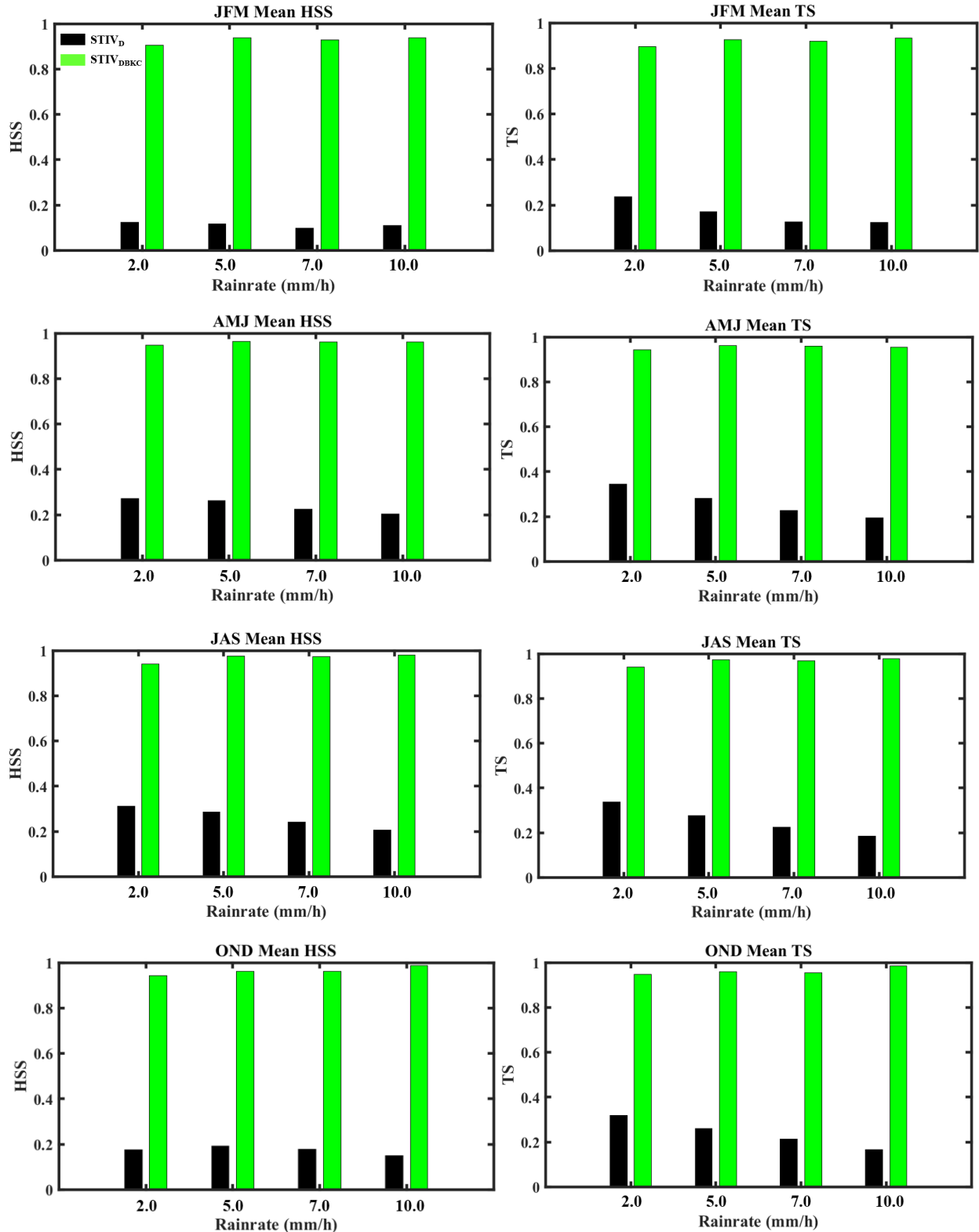


**Figure 10** – Seasonal mean HSS and TS statistics conditional on different rainfall thresholds for the entire network over the 10-year reference period (2008-2017). StageIV<sub>D</sub> (black); StageIV<sub>DBKC</sub> (green).

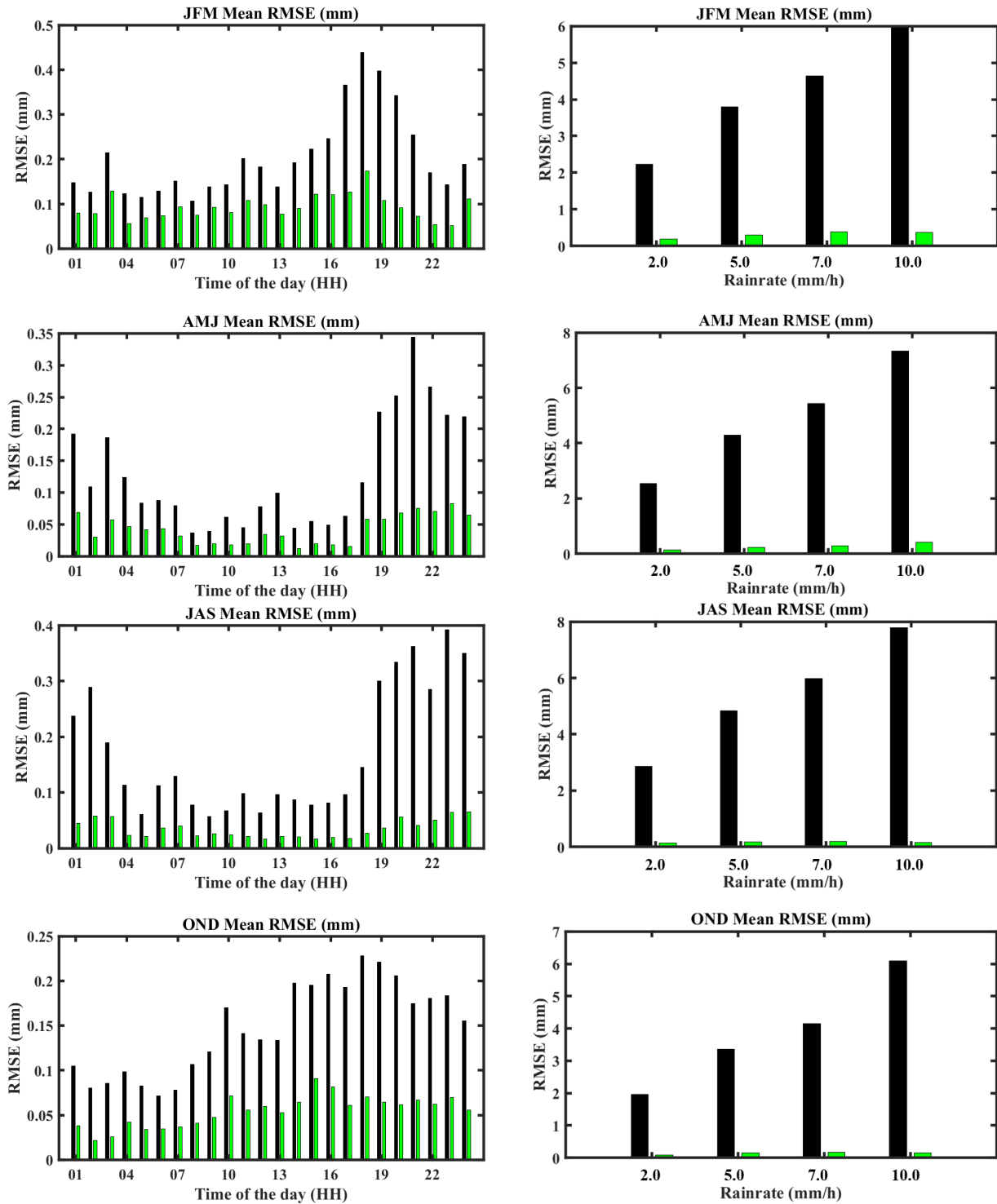


**Figure 11** – Diurnal cycle of RMSE at hourly time-scale and seasonal-scale RMSE conditional on observed rainfall rate StageIV<sub>D</sub> (black); StageIV<sub>DBKC</sub> (green).

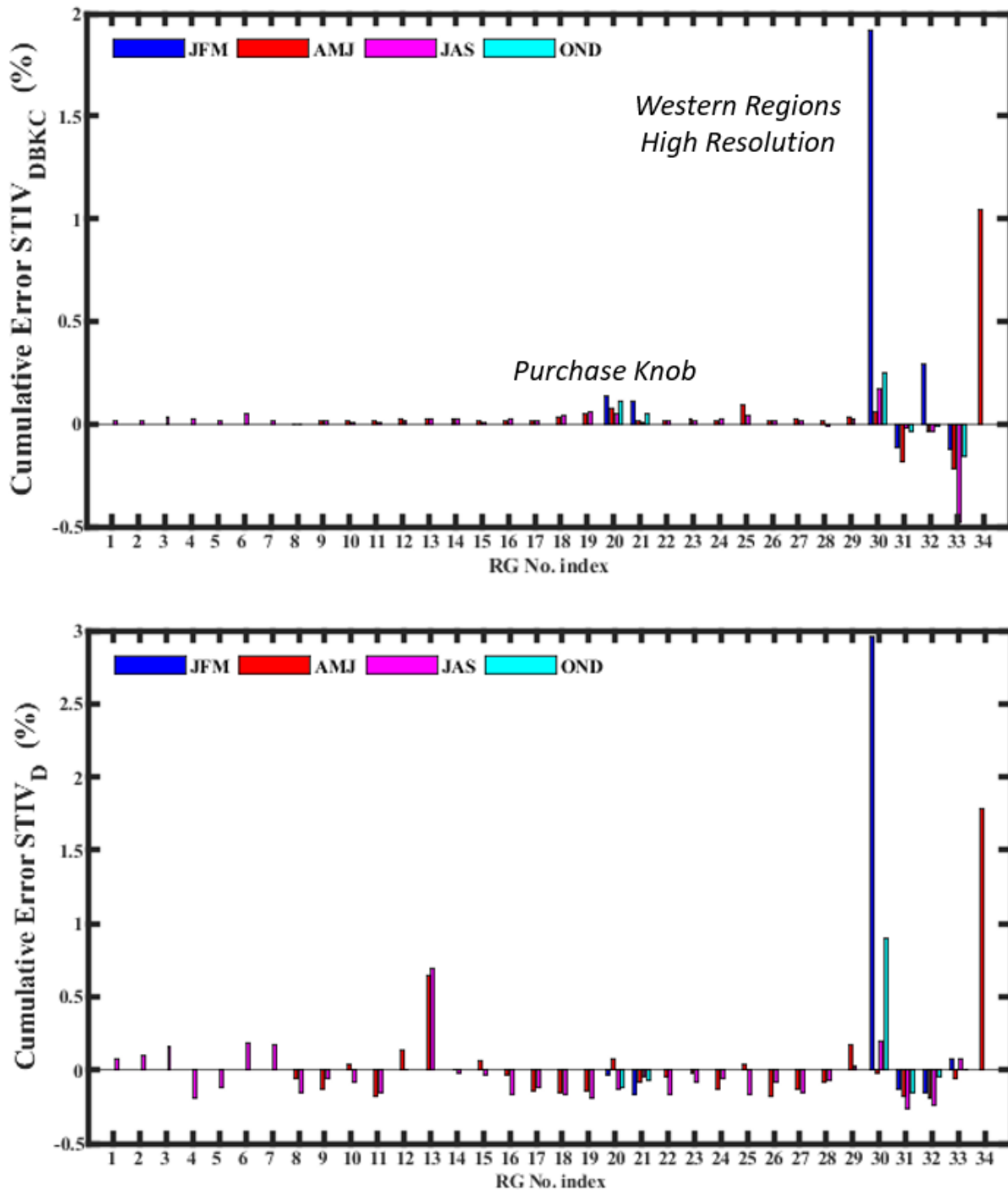


**Figure 12 –** Rainfall accumulation error for each gauge in Table 1 (RG Index) and as a function of season for StageIV<sub>DBKC</sub> (top panel) and StageIV<sub>D</sub> (bottom panel).

#### 4.4 Spatial variability and Orographic Modulation of Rainfall

For independent evaluation, three high-quality disdrometer stations (Figure 1, Table 2) among nine available during the IPHEX IOP are selected to illustrate the temporal evolution of rainfall

accumulations: P4 (elevation: 1956m) on the western ridges at high elevation, and P20 (elevation: 1860m) and P9 (elevation: 794m) in the inner region at high and low elevation respectively. Note that errors in disdrometer measurements are not explicitly addressed here, but they are expected to be larger for high intensity rainfall as well as for fog-haze-cap clouds conditions ( e.g. Angulo-Martinez and Barros, 2015) when numbers of small drops are very large (for example P4).

**Table 2** – Geographical coordinates of high quality Parsivel 2 disdrometer stations available during the IPHEX IOP and used for independent evaluation (see Figure 1).

NO.	Site Location	Sensor	Lat.	Lon.	Elev. (m)
1	P3	P2	35.586157	-83.072477	1493
2	P4	P2	35.558240	-83.494937	1956
3	P8	P2	35.804689	-82.660401	598
4	P9	P2	35.517746	-82.965553	794
5	P10	P2	35.306469	-83.201963	690
6	P15	P2	35.441441	-83.074138	992
7	P18	P2	35.315374	-82.871927	1720
8	P19	P2	35.576834	-82.775736	954
9	P20	P2	35.464401	-83.113492	1860

Figure 14 shows that STIV<sub>DBKC</sub> works better at P4 (high elevation on the western ridges) than P9 (low elevations in the inner region). STIV<sub>DBKC</sub> overestimates low elevation rainfall associated with small scale afternoon convection that is not observed at low elevations. This is illustrated by the much steeper slopes at P9 as well as number of events. The performance at P20 shows the problems with overestimation of the large storm on May 15<sup>th</sup> on the lee side of one of the central ridges with respect to the propagating storm, which is aggravated by bias correction and kriging (i.e. Stage IV<sub>D</sub> is better than StageIV<sub>DBK</sub>), that is StageIV<sub>DBKC</sub> is overcorrecting localized rainshadow effects. Nevertheless, overall the product shows the ability to capture the overall frontal storm and also light rainfall but with different error patterns.

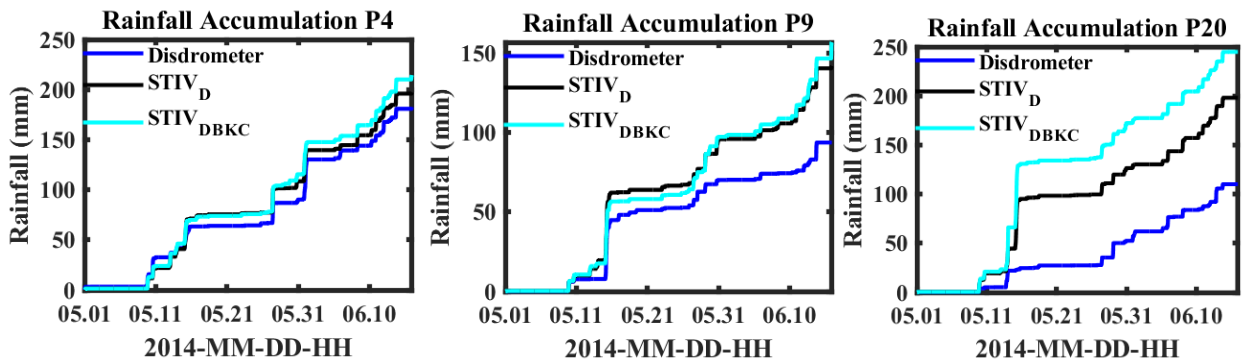


**Figure 14** - Cumulative rainfall curves at selected disdrometer locations (see Fig.1, Table 2) during the IPHEX IOP.

One way to illustrate this point is to characterize the dependence of the bias factor B with elevation calculated as follows:

$$B = \frac{\sum D \text{ or } RG}{\sum STIV_{DBKC}} \quad (25)$$

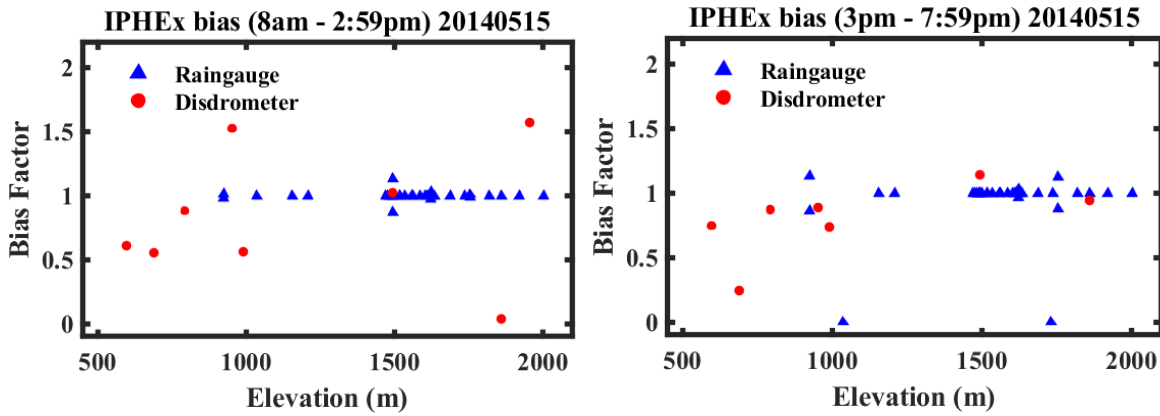


**Figure 15** – Bias factor at different locations for a frontal storm on May 15, 2014 during the IPHEX IOP: left panel: morning and early afternoon; right panel: afternoon and early evening.

For an event with strong large-scale organization, raingauges and disdrometers can capture the rainfall most of the time, and as expected the performance is very good at the raingauge locations during the frontal passage in the morning (Figure 15). Overall, STIV<sub>DBKC</sub> overestimates at the disdrometer locations at lower elevations as indicated by  $B < 1$ . Similar analysis for a day characterized by isolated precipitation (5/27/2014) is presented in Figure 16.

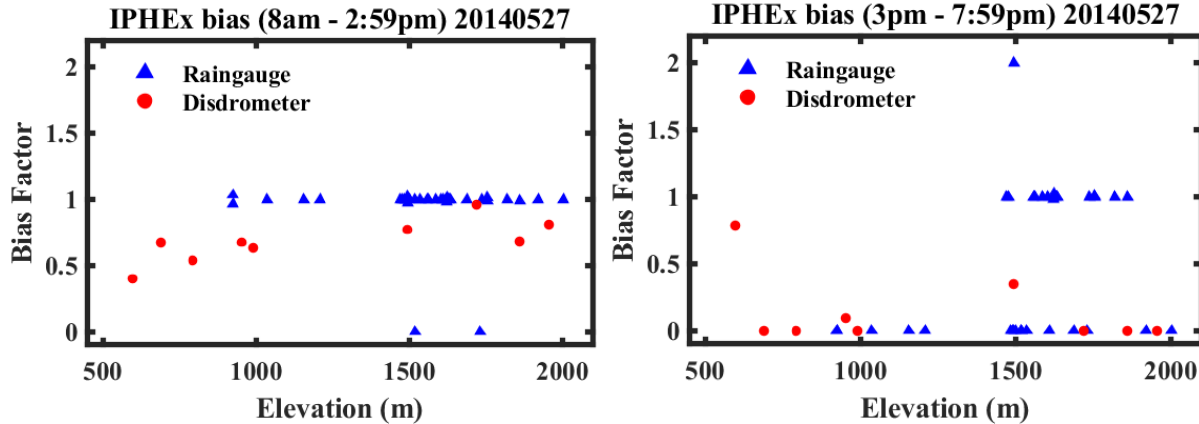


**Figure 16** - Bias factor at different locations for multiple clusters of convective rainfall in the absence of synoptic forcing.

For days with isolated thunderstorms in the afternoon and light rainfall in the morning, STIV<sub>DBKC</sub> overestimates rainfall everywhere except at the gauge locations that are co-located with the thunderstorm activity. This analysis suggest that the current IPHEX RQPE product will need to address three critical overestimation issues:

- 1) Localized mesoscale upwind-leewind effects (rainshadow) during synoptic scale events;
- 2) Overestimation at low elevations during synoptic scale events;
- 3) Spatial intermittency tied to isolated convective activity.

## **5. Conclusion**

Radar products have insufficient resolution for comparison against raingauges. A fractal downscaling framework is used to preserve the spatial statistics of rainfall fields and obtain high resolution data sets. Subsequent results have shown that radar data contain significant biases especially in complex terrain. Bias correction and Kriging are then applied to reduce the biases in the radar rainfall products. Significant biases in StageIV<sub>D</sub> are removed during the late afternoon. And these techniques have well solved the problem of high biases over western ridges. A ten year climatology analyses indicate that previous bias correction is not sufficient, therefore a slight and extreme rainfall correction are employed in bias correction scheme. Results suggest that the application of this scheme can greatly reduce biases in StageIV<sub>D</sub> in terms of missing precipitation, providing us an unambiguous method to correct radar biases especially at high elevations. Performance metrics such as Threat Score (TS) and Heidke Skill Scores (HSS) are on average  $> 0.8$  and close to 1 respectively for various rainfall thresholds over the 10-year period, and  $> 0.5$  at the event time-scale(hourly). The root mean square error (RMSE) at the gauges is below 0.1 mm/hr and 0.5% for seasonal-scale accumulations. Evaluation against an independent disdrometer data set consisting of disdrometers at various locations indicates large overestimation errors ( $\sim 30\%$ ) in the inner mountain region and at low elevations during the IPHEX IOP. Error analysis shows that overestimation is tied to leeside and low elevation rainfall organized by ridge-valley features in the inner mountain region during the passage of synoptic scale events, and to unwarranted space-filling when only isolated convective activity is present. Based on this, a Version 2 product will be focus on correcting low elevation rainfall using information from low elevation disdrometers and from NWP model simulations. Spatial intermittency will be addressed through modified fractal downscaling methodology conditional on the perimeter of precipitation features (i.e rain support of rainfall clusters in Nogueira and Barros, 2015) in StageIV.

## **Acknowledgements**

The work was supported by NASA Precipitation Measurement Mission Program under NASA grant NNX16AL16G with the second author and a NASA Earth System Science Fellowship with the first author. The authors acknowledge Malarvizhi Arulraj for her help and advice, and Anna M. Wilson, Gregory Cutrell and Douglas Miller and his team of students at UNC Asheville for collecting and calibrating the raingauge data sets used here.

## References

- Anagnostou, E.N., Morales, C.A., Dinku, T., 2001. The use of TRMM precipitation radar observations in determining ground radar calibration biases. *J. Atmos. Ocean. Technol.* 18 (4), 616–628.
- Angulo-Martinez, M, and Barros, A.P., 2015. Measurement Uncertainty in rainfall kinetic energy and intensity relationships for soil erosion studies: an evaluation using PARSIVEL disdrometers in the Southern Appalachian Mountains. *Geomorphology*, 228, 28-40, DOI:10.1016/j.geomorph.2014.07.036.
- Arulraj, M., and Barros, A.P., 2017. Shallow precipitation detection and classification using multifrequency radar observations and model simulations. *J. Atmos. Ocean. Technol.*, 34, pp. 1963-1983, <https://doi.org/10.1175/JTECH-D-17-0060.1>.
- Arulraj, M., and Barros, A.P., 2019. Improving quantitative precipitation estimates in mountainous regions by modelling low-level seeder-feeder interactions constrained by Global Precipitation Measurement Dual-frequency Precipitation Radar measurements. *Remote Sensing of Environment* 231, <https://doi.org/10.1016/j.rse.2019.111213>.
- Barros, A.P., Malarvizhi Arulraj, Anna M. Wilson, Douglas Miller, Gregory Cutrell, Paul Super, and Walter A. Petersen. 2017. “IPHEx-Southern Appalachian Mountains -- Rainfall Data 2008-2014”. <https://doi.org/10.7924/G8CJ8BJK>.
- Barros A.P., Petersen W, Schwaller M, Cifelli R, Mahoney K, Peters-Liddard C, Shepherd M, Nesbitt S, Wolff D, Heymsfield G, Starr D. 2014. NASA GPM-Ground Validation: Integrated Precipitation and Hydrology Experiment 2014 Science Plan. EPL/Duke University (Pub.): 64pp. <http://dx.doi.org/10.7924/G8CC0XMR>.
- Barros, A.P., Tao, K., 2008. A space-filling algorithm to extrapolate narrow-swath instantaneous TRMM microwave rain-rate estimates using thermal IR imagery. *J. Atmos. Oceanic Technol.* 25, 1901–1920. <https://doi.org/10.1175/2008JTECHA1019.1>.
- Bailey, T. C., & Gatrell, A. C., 1995. Interactive spatial data analysis (Vol. 413). Essex: Longman Scientific & Technical. 109-111.
- Bindlish, R., Barros, A.P., 1996. Aggregation of digital terrain data using a modified fractal interpolation scheme. *Comput. Geosci.* 22 (8), 907–917. [https://doi.org/10.1016/S0098-3004\(96\)00049-0](https://doi.org/10.1016/S0098-3004(96)00049-0).
- Bindlish, R., Barros, A.P., 2000. Disaggregation of rainfall for one-way coupling of atmospheric and hydrological models in regions of complex terrain. *Global Planet. Change*, 25 (12), 111–132. [https://doi.org/10.1016/S0921-8181\(00\)00024-2](https://doi.org/10.1016/S0921-8181(00)00024-2).

Borga, M., Tonelli, F., 2000. Adjustment of range-dependent bias in radar rainfall estimates. *Phys. Chem. Earth B – Hydrol. Oceans Atmos.* 25 (10–12), 909–914.

Diggle, P. and Ribeiro, P. J., 2007. *Model-based geostatistics*. Springer Series in Statistics, 230.

Duan, Y. and Barros, A. P. 2017. Understanding How Low-Level Clouds and Fog Modify the Diurnal Cycle of Orographic Precipitation Using In Situ and Satellite Observations, *Remote Sens.*, 9, 920, <https://doi.org/10.3390/rs9090920>.

Duan, Y., Wilson, A. M., and Barros, A. P. 2015. Scoping a field experiment: error diagnostics of TRMM precipitation radar estimates in complex terrain as a basis for IPHEx2014, *Hydrol. Earth Syst. Sci.*, 19, 1501–1520, <https://doi.org/10.5194/hess-19-1501-2015>.

Gabella M, Joss J, Perona G. 2000. Optimizing quantitative precipitation estimates using a noncoherent and a coherent radar operating on the same area. *J. Geophys. Res.* 105: 2237-2245

Hubert, P., and Coauthors, 1993. Multifractals and extreme rainfall events. *Geophys. Res. Lett.*, 20, 931–934.

Kim, G., and Barros, A.P., 2001. Quantitative Flood Forecasting Using Multisensor Data and Neural Networks. *J. Hydrology*, 246, 45-62.

Krajewski WF, Georgakakos KP. 1987. Cokriging radar-rainfall and rain gauge data. *J. Geophys. Res.* 21: 764-768.

Lavallée, D., S. Lovejoy, and D. Schertzer, 1991b. Universal multifractal theory and observations of land and ocean surfaces, and of clouds. Wave Propagation and Scattering in Varied Media II, V. K. Varadan, Ed., International Society for Optical Engineering (SPIE Proceedings, Vol. 1558), 60–75.

Lavallée, D., Lovejoy, S., Schertzer, D., Ladoy, P., 1993. Nonlinear variability and Landscape topography: analysis and simulation. In: De Cola, L., Lam, N. (Eds.), *Fractals in Geography*. PTR, Prentice Hall, pp. 158–192.

Li, J., & Heap, A. D. 2008. A review of spatial interpolation methods for environmental scientists. 11-12.

Lin, Y. and Mitchell, K. E., 2005: The NCEP stage II/IV hourly precipitation analyses: development and applications. 19th Conference on Hydrology, San Diego, CA, Amer. Meteor. Soc. 1.2, [https://ams.confex.com/ams/Annual2005/techprogram/paper\\_83847.htm](https://ams.confex.com/ams/Annual2005/techprogram/paper_83847.htm).

Mälicke, M., Hassler, S. K., Weiler, M., Blume, T., and Zehe, E. 2018. Exploring hydrological similarity during soil moisture recession periods using time dependent variograms, *Hydrol. Earth Syst. Sci. Discuss.*, <https://doi.org/10.5194/hess-2018-396>.

McBratney AB, Webster R. 1986. Choosing functions for semivariograms of soil properties and fitting them to sampling estimates. *Journal of Soil Science* 37: 617–639.

McBride, J. L., and E. E. Ebert, 2000. Verification of quantitative precipitation forecasts from operational numerical weather prediction models over Australia. *Wea. Forecasting*, 15, 103–121.

Nelson, B.R., Seo, D.J., Kim, D., 2010. Multisensor precipitation reanalysis. *J.Hydrometeorol.* 11 (3), 666–682.

Nogueira, M. and A. Barros., 2015. Transient stochastic downscaling of quantitative precipitation estimates for hydrological applications. *Journal of Hydrology* 529: 1407-1421.

Prat, O.P., Barros, A.P., 2010a. Assessing satellite-based precipitation estimates in the Southern Appalachian mountains using rain gauges and TRMM PR, *Adv. Geosci.*, 25, pp. 143-153, <https://doi.org/10.5194/adgeo-25-143-2010>.

Prat, O.P., Barros, A.P., 2010b. Ground observations to characterize the spatial gradients and vertical structure of orographic precipitation – experiments in the inner region of the Great Smoky Mountains. *J. Hydrol.* 391 (1–2), 141–156. <https://doi.org/10.1016/j.jhydrol.2010.07.013>.

Rebora, N., von Ferraris, L., Hardenberg, J., Provenzale, A., 2006. RAINFARM: rainfall downscaling by a filtered autoregressive model. *J. Hydrometeor.* 7, 724–738.

R.A. Fulton, J.P. Breidenbach, D.J. Seo, D.A. Miller, T. O'Bannon, 1998. The WSR-88D rainfall algorithm *Weather Forecast.*, 13 (2), pp. 377-395

Schertzer, D., and S. Lovejoy, 1987: Physical modeling and analysis of rain and clouds by anisotropic scaling multiplicative processes. *J. Geophys. Res.*, 92, 9693–9714.

Seo, B.-C., et al. (2018). "Comprehensive Evaluation of the IFloodS Radar Rainfall Products for Hydrologic Applications." *Journal of Hydrometeorology* 19(11): 1793-1813.

Seo DJ, Breidenbach JP. 2002. Real- time correction of spatially nonuniform bias in radar rainfall data using rain gauge measurements. *J. Hydrometeorol.* 3: 93–111.

Seo DJ, Krajewski WF, Bowles DS. 1990. Stochastic interpolation of rainfall data from rain gauges and radar using cokriging. 1. Design of Experiments. *Water Resources Research* 26: 469–477.

Sideris, I., Gabella, M., Erdin, R., & Germann, U. 2014. Real-time radar-rain-gauge merging using spatio-temporal co-kriging with external drift in the alpine terrain of Switzerland. *Quarterly Journal of the Royal Meteorological Society*, 140(680), 1097-1111.

Steiner, M., Smith, J.A., Burges, S.J., Alonso, C.V., Darden, R.W., 1999. Effect of bias adjustment and rain gauge data quality control on radar rainfall estimation. *Water Resour. Res.* 35 (8), 2487–2503.

Sun, X., and A. P. Barros, 2010. An evaluation of the statistics of rainfall extremes in rain gauge observations, and satellite-based and reanalysis products using universal multifractals. *J. Hydrometeor.*, 11, 388–404, <https://doi.org/10.1175/2009JHM1142.1>.

Tao, K., Barros, A.P., 2010. Using fractal downscaling of satellite precipitation products for hydrometeorological applications. *J. Atmos. Oceanic Technol.* 27, 409–427. <https://doi.org/10.1175/2009JTECHA1219.1>.

Tao, J. and Barros, A.P., 2013. Prospects for flash flood forecasting in mountainous regions - An investigation of Tropical Storm Fay in the Southern Appalachians, *Journal of Hydrology*. 69-89. <https://doi.org/10.1016/j.jhydrol.2013.02.052>.

Villarini, G., Krajewski, W.F., 2010. Review of the different sources of uncertainty in single polarization radar-based estimates of rainfall. *Surv. Geophys.* 31 (1), 107–129.

Wang CC, 2014. On the calculation and correction of equitable threat score for model quantitative precipitation forecasts for small verification areas: the example of Taiwan. *Weather Forecast* 29(4):788–798.

Wang, J. and Wolff, D.B., 2010. "Evaluation of TRMM ground-validation radar-rain errors using rain gauge measurements." *Journal of Applied Meteorology and Climatology* 49(2): 310-324.

Wilson, A. M., and A. P. Barros, 2014. An investigation of warm rainfall microphysics in the southern Appalachians: Orographic enhancement via low-level seeder–feeder interactions. *J. Atmos. Sci.*, 71, 1783–1805, <https://doi.org/10.1175/JASD-13-0228.1>.

Zhang, J., Howard, K., Langston, C. and many others, 2014. Multi-Radar Multi-Sensor (MRMS) Quantitative Precipitation Estimation - Initial Operating Capabilities, BAMS, <https://doi.org/10.1175/BAMS-D-14-00174.1>